

Nanoscale Characterizations of Plasmon-Mode Superposition in Iron-Filled Multiwalled Carbon Nanotubes

Dong Yang, Dingguo Zheng,* Siyuan Huang, Wentao Wang, Jun Li, Shuaishuai Sun, Jiangbo Lu, Jieshan Qiu, Huanfang Tian, Jianqi Li,* and Huaixin Yang*



Cite This: *Nano Lett.* 2025, 25, 9670–9676



Read Online

ACCESS |



Metrics & More



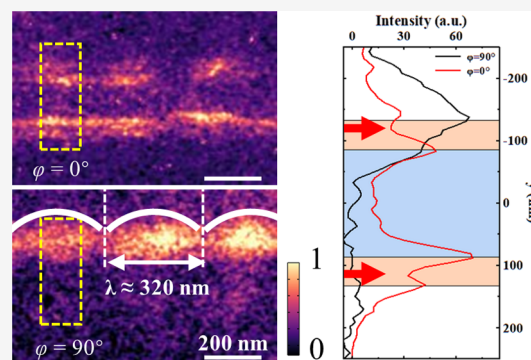
Article Recommendations



Supporting Information

ABSTRACT: The coaxial plasmonic waveguide structure has unique advantages in nanophotonics. This study provides insight into high-resolution images of the plasmonic near-field of iron-filled multiwalled carbon nanotubes, as observed through photon-induced near-field electron microscopy. The images reveal plasmon interference between the iron core and the carbon nanotube and the superposition of polarization-dependent plasmon modes. Under specific phase differences between plasmon modes, these modes show asymmetric near-field contrast when the dipole field is perpendicular to the electron beam and a pronounced low-intensity channel when parallel. Finite-element simulations further support the analysis, providing insights into the plasmon-mode superposition within the coaxial structure. This comprehensive understanding of plasmon modes in metal-filled nanotubes paves the way for advanced applications in nanosensors and nanowaveguides.

KEYWORDS: *high-resolution plasmonic image, buried field, coaxial structure, iron-filled MWCNTs, PINEM*



The plasmons of the coaxial structure exhibit a high mode density and support local Fabry–Perot plasmon resonances,¹ characterized by strong localization. These distinctive properties have garnered significant attention, particularly in the design of metamaterials with negative refractive indexes.^{2,3} As a result, the nanoscale characterization of plasmons and the analysis of their modes in complex systems have become increasingly critical. A variety of advanced experimental techniques, such as near-field scanning optical microscopy (SNOM),^{4–6} photoemission electron microscopy (PEEM), electron energy loss spectroscopy (EELS),^{7,8} have been employed to investigate the spatiotemporal properties of plasmonic near-field. For SNOM, minute probes are required to locally enhance an electromagnetic field through a complex interplay between surface plasmon (SP) excitation and localization of electric charges by geometrical singularities.⁵ The amplitude and phase information can be obtained by analyzing the scattered light field.⁹ PEEM can obtain more information about electrons that overflow from the surface after photoexcitation.¹⁰ EELS demonstrates the ability to excite the full set of localized surface plasmon resonance (LSPR) modes by high-energy electrons.¹¹ However, the direct observation of plasmonic near-field distributions in complex systems with sub-100 nm spatial resolution remains challenging.

Photon-induced near-field electron microscopy (PINEM) has emerged as a novel method to explore electron–photon interactions at nanoscale and femtosecond domains^{12,13} and

found widespread application in imaging SPs in various nanostructures such as nanoparticles,^{14,15} metallic nanowires,^{12,16} carbon nanotubes,^{17,18} nanotips,¹⁹ rough metallic films,^{20,21} and biological samples.^{22,23} Additionally, it facilitates the study of near-field coupling between dimers like copper bowtie²⁴ and entangled nanoparticles.²⁵ The near-field characteristics of entangled silver nanoparticles reported by Zewail’s team showed void-channels as narrow as 6 nm, demonstrating the spatial resolution capability of PINEM.²⁵ Moreover, because high-energy electron probes can interact with photons as they penetrate the sample, PINEM holds the capacity to image the buried near-field.²⁶

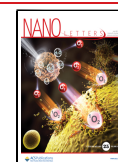
In this study, we report observations of the plasmonic near-field and the optical polarization dependence of iron-filled multiwalled carbon nanotubes (MWCNTs) by PINEM. Metal-filled carbon nanotubes (CNTs) have extensive applications across various domains, including nanodevices, high-density magnetic memory,²⁷ electrochemistry,^{28–31} spintronics,³² microwave absorption,^{33,34} sensors, biomedicine, flexible materials,³⁵ and a plasmon-enhanced photodetector.^{36–38} In a coaxial structure, MWCNTs can isolate the core from the

Received: March 11, 2025

Revised: May 30, 2025

Accepted: May 30, 2025

Published: June 4, 2025



environment, thereby protecting it from oxidation.³⁹ When compared to noble metals, which are considered excellent plasmonic materials, iron (Fe) exhibits a higher dissipation (a larger imaginary part of the refractive index), resulting in relatively weaker but still visible plasmon signals.^{40–42} Ferromagnetic metals like Fe, Co, and Ni also show promise in nanooptics due to their unique ability to combine magnetic properties with plasmonic behavior.

Here, we investigate the near-field interference between the metal core and the MWCNT in the coaxial structure as well as the superposition of plasmon modes by imaging the plasmonic near-field of MWCNTs partially and fully filled with iron. This analysis was complemented by finite-element simulations, which further confirmed the influence of polarization on the superposition mechanism of the plasmon modes of the coaxial structure.

Figure 1 presents the microstructure and chemical state of the iron-filled MWCNTs. Iron was introduced to the

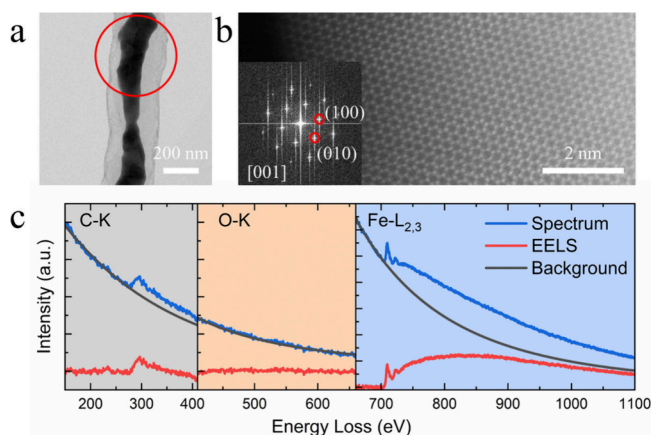


Figure 1. Microstructure and EELS characteristics of the iron-filled MWCNTs. (a) TEM image of iron-filled MWCNTs. Iron is filled inside the hollow MWCNTs, forming nanorods with a diameter of about 100 nm. The shape and distribution are related to the geometry inside the MWCNTs. (b) HAADF-STEM and FFT images of ϵ -Fe along the [001] direction. (c) EELS of iron-filled MWCNTs, acquired from the red circular region of part a. The element characteristic peaks are indicated in colored areas.

nanopores of MWCNTs via a vapor diffusion method,⁴³ as shown in Figure 1a. The results of high-angle annular dark-field scanning transmission electron microscopy (HAADF-STEM) and fast Fourier transform (FFT) reveal that the iron filled in MWCNTs adopts a hexagonal structure ϵ -Fe, with images along the [001] direction depicted in Figure 1b. The presence of ϵ -Fe is attributed to the internal pressure provided by the MWCNTs.^{44,45} Furthermore, the MWCNTs effectively protect the iron from oxidation when exposed to air for prolonged periods, ensuring that the dielectric properties of the iron core at high frequencies are consistent with the typical behavior of metals. As shown in Figure 1c, no O–K-edge prepeak appears, indicating that no oxidation of the iron core occurs.

Figure 2 depicts nanoscale characterizations of the photo-induced plasmonic near-field of partially iron-filled MWCNTs. A schematic diagram of the interaction between electron pulses and the specimen irradiated by femtosecond pulses (pump laser) is shown in Figure 2a. The pump laser incidence direction is perpendicular to the electron beam with the sample holder rotated 25° away from the Y axis. The setup of the

optical and electric components is described in the Supporting Information. In previous studies, it has been established that pulsed electrons via the optical near-field can be strongly modulated by absorbing or emitting photons with an energy quanta of $n\hbar\omega$, where n is an integer, \hbar is the reduced Planck constant, and ω is the frequency of the pump laser. The probability P_n of absorbing or emitting n photons is given by the square of the n th-order Bessel function of the first kind:⁴⁶ $P_n(x, y) = J_n^2(2|g|)$, where g is defined as $g = \frac{e}{\hbar\omega} \int_{-\infty}^{+\infty} E_z(x, y, z) e^{-i(\omega/v_e)z} dz$, in which e is the electron charge, v_e is electron speed, and $E_z(x, y, z)$ represents the electric field component along the electron-beam direction.

The energy change of the pulsed electrons after being modulated by the near-field is realized by the EELS sidebands. Figure 2b shows the time-resolved EELS after normalization. At 0.6 ps, only the zero-loss peak is observed, whereas at 0 ps, an energy comb formed by electrons modulated by strong plasmonic near-fields becomes visible. The energy state has a slight slip due to dispersive propagation of the electron pulse. Energy-gain electrons, selected through an energy filter, are used for imaging to reveal the plasmonic near-field distribution, as shown in Figure 2c. The near-field distribution exhibits a wavelike structure when the external instantaneous electric field is parallel to the MWCNTs (left) and a uniform distribution when the electric field is perpendicular to the MWCNTs (right). Additionally, a stronger localized plasmonic near-field is observed around the iron nanorods. This also shows that the presence of the iron core significantly enhances the plasmon effect of MWCNTs (Figure S1). High-energy electron probes pass through the MWCNTs and are modulated by the plasmonic near-field between the iron core and the CNT walls embedded inside the MWCNTs. This demonstrates that PINEM can enable visualization of the buried fields. For a study of the dynamics, the time-resolved EELS in Figure 2b shows that the entire evolution process is the result of the combined effects of electron pulse, pump pulse, and plasma duration. This is consistent with the energy-filtered transmission electron microscopy (EFTEM) dynamic results, as shown in Figure S2. The dynamic changes of the iron core and the different characteristic regions of the MWCNT show a consistent behavior.

Building upon PINEM's capability to probe buried electromagnetic fields, we undertake an in-depth study of the plasmonic near-field interference in coaxial structures. In particular, iron is fully filled within the MWCNTs, as shown in Figure 3a. The diameter of the iron nanorods is 148 ± 18 nm (Figure S3), while the outer diameter of the MWCNTs is about 270 nm. Plasmonic near-fields can be induced by a laser at both the interface between the iron core and MWCNT and the interface between the MWCNT and vacuum. When the thickness of the MWCNT layers becomes comparable to or less than the decay length of the near-field on the iron core, interference of the plasmonic near-fields appearing at the two interfaces will occur.

Parts b and c of Figure 3 illustrate the interference of plasmonic near-fields appearing at the two interfaces and its variation with polarization. It is intriguing that, in Figure 3b, a low-intensity channel with a peak-to-peak distance of approximately 40 nm (illustrated by the red line in Figure 3d) appears in the interlayer region of the MWCNT when the polarization is parallel to the electron beam. As polarization is adjusted, the overall PINEM contrast decreases, and the low-

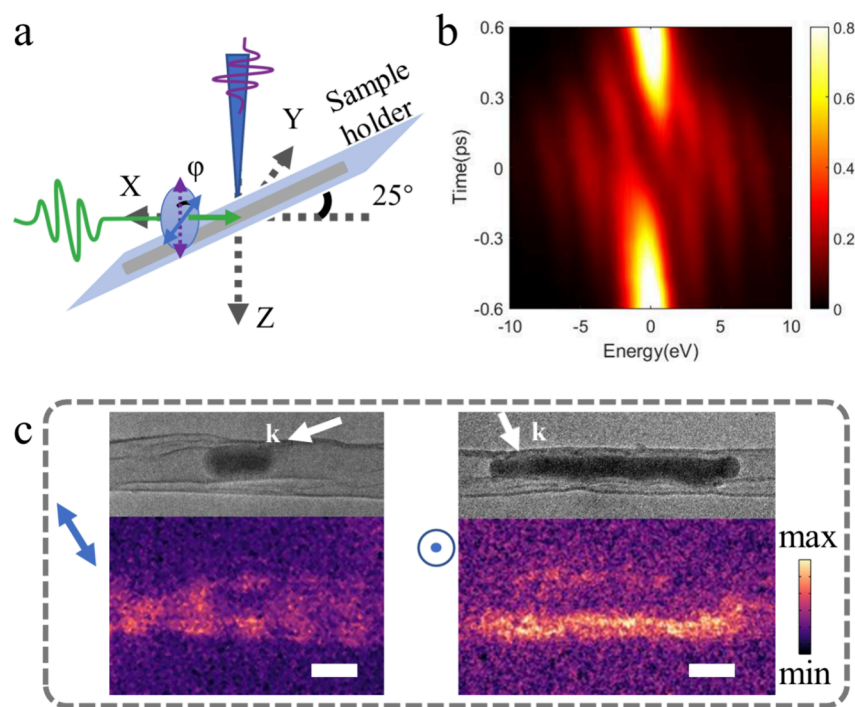


Figure 2. Plasmonic near-field characterization of the partially iron-filled MWCNTs. (a) Schematic diagram of the optical and electric components of the PINEM system. The polarization direction of the pump laser is parallel to the electron-beam direction when $\varphi = 0^\circ$ and perpendicular to the electron-beam direction when $\varphi = 90^\circ$. (b) Electron populations in different quantum states for iron-filled MWCNTs. (c) Bright-field images and corresponding EFTEM images of partially iron-filled MWCNTs, obtained with an energy-filtering window of -5 to -25 eV. The scale bar is 200 nm. The polarization of the pump laser is indicated on the left side of the images, and the white arrows indicate the direction of laser incidence. The intensity in each panel is independently scaled for clarity.

intensity channels disappear. At a polarization angle of $\varphi = 90^\circ$, as shown in Figure 3c, the near-field image distinctly reveals the formation of standing waves with a wavelength of approximately 320 nm (considering the tilt of the sample holder at 25° and correcting it to 353 nm), which appears only in the front surface of the iron core. This one-sided near-field extinction is observed only under specific polarization conditions (illustrated by the black line in Figure 3d). In hollow MWCNTs, a similar one-sided contrast disappearance also exists (Figure S1).

These near-field patterns arise from the interference of electromagnetic fields of different plasmon modes, controlled by polarization. To further understand this phenomenon, we perform an analysis of the plasmon modes in the cylindrical coaxial structure. In our nanotubes, at least three resonance modes are observed: monopole (TM_0) and dipole (HE_1^y and HE_1^z). The theoretical results of mode analysis are given in Figure 4a.

At TM_0 mode, the SP field distribution on the MWCNTs surface is perfectly symmetric between the front and back surfaces. In contrast, in the HE_1 mode, there is a phase difference of π between the SP field distributions on the front and back surfaces of the MWCNTs, and the electric-field directions are opposite (Figure S5). As shown in Figure 4b, the contribution of the TM_0 mode to the electron–photon coupling is symmetrical, while the contribution of the HE_1^y mode results in opposite signs. As for HE_1^z , which has a phase difference of $\pi/2$ with HE_1^y , showing symmetry in the contribution to the coupling intensity, the sign is opposite that of TM_0 . Interestingly, the HE_1^z mode induces much larger E_z than the HE_1^y mode; however, the coupling strength of the HE_1^z mode is much smaller than the HE_1^y mode. This is because

of the different matching degrees of the optical phase velocity to free electron group velocity at the different mode. In addition, if the core is replaced by a noble metal (e.g., silver) in our simulation, a stronger SP near-field will appear between the noble metal and the CNT, but this may prevent us from clearly seeing the low-intensity channel (Figure S6).

When the TM_0 and HE_1^y modes coexist, the destructive interference of the SP fields on the back surface cancels each other out, while the instructive interference of the SP fields on the front surface reinforces each other. This leads to an asymmetric distribution of the coupling strength. When the TM_0 and HE_1^z modes coexist, the coupling strength on both sides decreases, but the symmetry is still maintained. Parts c and d of Figure 4 display variation of the electron–photon coupling intensity $|g|$ along the y direction of the superposition mode. The superposition of TM_0 and HE_1^y leads to a one-sided contrast when the dipole field is perpendicular to the electron-beam direction (Figure 4c), while the superposition of TM_0 and HE_1^z consistently results in a symmetrical image when the dipole field is parallel to the electron-beam direction (Figure 4d).

In a previous report, a void-channel appears due to the entanglement of two silver particles.²⁵ This channel is formed by the coherent superposition of electric fields originating from two particles with equal amplitudes and opposite directions. However, the near-field interference of iron-filled MWCNTs will be more complex because of the dielectric properties and geometry structure in the two-layer coaxial plasmon waveguide structure. In addition to the coherent superposition of different plasmon modes, it is also essential to consider the potential phase difference between the various modes along the axial direction. The superposition of modes depends not only on

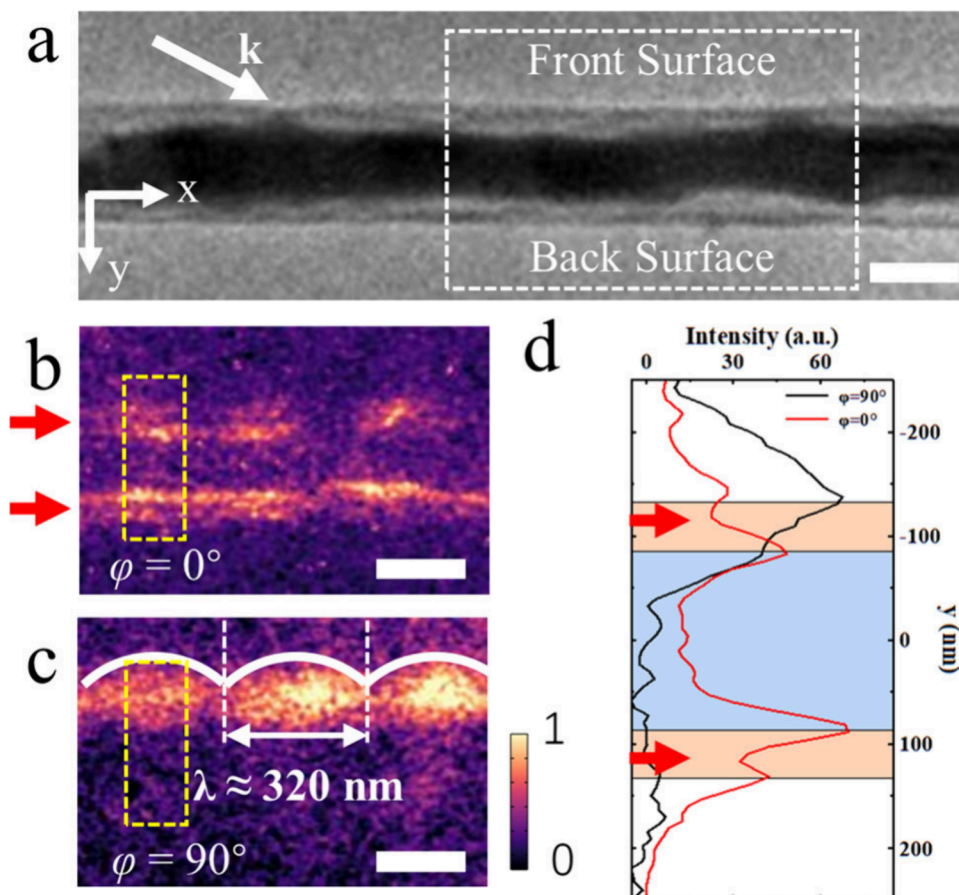


Figure 3. Polarization dependence of the plasmonic near-field. (a) Bright-field image of iron fully filled within the MWCNT. The white arrow indicates the direction of laser incidence, projected onto the X – Y plane, marking an angle of 20° with respect to the axis of the MWCNT. (b and c) Series of EFTEM images taken from the white rectangle region in part a, with energy filtering between -5 and -25 eV (i.e., $n = 2$ – 10). The corresponding optical polarization angles (φ) are denoted in the bottom left. Here, $\varphi = 0^\circ$ represents optical polarization parallel to an electron beam. The red arrows in parts b and d highlight the locations of low-intensity channels. The scale bar is 200 nm. Parts b and c are normalized to the same intensity scale. The images under other polarization conditions are shown in Figure S4. (d) Line profiles extracted from the yellow dashed box on parts b and c. The orange areas correspond to the MWCNT, and the blue area corresponds to iron.

their relative proportion but also on the phase difference. This electron–photon coupling strength of the superposition field is

$$|g(x, y)| = |\gamma_{\text{TM}_0} g_{\text{TM}_0} + \gamma_{\text{HE}_1} e^{i\theta} e^{i\phi} g_{\text{HE}_1}|$$

Here γ is the relative proportion of eigenmode and θ is the phase difference between the TM_0 and HE_1 modes. The second term indicates the contribution of the HE_1^y (HE_1^z) mode to the coupling strength when $\phi = 0$ ($\phi = \pi/2$). The phase difference ($\theta = 0.41\pi$) causes the intensity of the electron–photon coupling along y direction, resulting in a noticeable low-intensity channel, as shown in Figure 4d. The simulation results of other phases are shown in Figure S7. As can be seen from Figure 4b, the coupling strength of the electron–photon coupling in a single mode shows a tendency to decay to the distance, which is consistent with the characteristics of the electric-field distribution. The phase difference between different modes changes the phase matching, resulting in a phase mismatch between the two interfaces, which is manifested as the electrons not always being in an accelerated or decelerated state. Therefore, there is a decrease in the coupling strength between the two interfaces.

This polarization-dependent near-field feature is present not only in fully iron-filled MWCNT structures but also in partially

iron-filled MWCNTs. As demonstrated in the experimental results shown in Figure 5, the plasmonic near-field can be effectively tuned by aligning the dipole field with the direction of the external electric field. When the dipole field is oriented perpendicular to the electron beam, a one-sided near-field image is observed. Furthermore, reversing the dipole-field results in an axial shift of the near-field by a phase of π , with the surface of destructive interference switching sides. In contrast, when the dipole field is aligned parallel to the electron beam, the near-fields on both sides of the MWCNT exhibit symmetrical distributions.

In conclusion, we directly observed the buried near-field of the plasmon of iron-filled MWCNTs. In the coaxial structure, there is not only near-field interference between the core and the MWCNT but also polarization-dependent plasmon-mode superposition. When the dipole field is perpendicular to the electron beam, the coherent superposition of the TM_0 and HE_1^y modes leads to the disappearance of asymmetric PINEM contrast. In contrast, when the dipole field is parallel to the electron beam, the PINEM contrast remains symmetric. However, the coherent superposition of the TM_0 and HE_1^z modes, influenced by an axial phase difference, results in a distribution of electron–photon coupling strength along y , creating a low-intensity channel due to destructive interference.

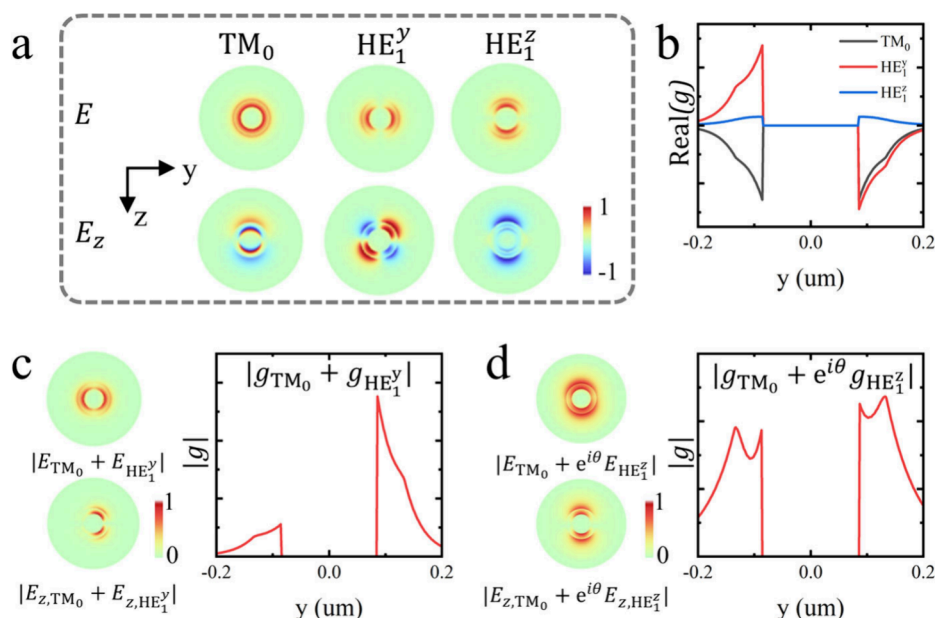


Figure 4. Finite-element analysis of mode hybridization and superposition revealed by PINEM. (a) Hybridization electric field E distribution of the coaxial structure and z component of the electric field E_z distribution. The intensities are normalized separately. (b) Coupling strength $\text{Re}(g)$ of three plasmonic eigenmodes. The coupling strength of superposition modes at (c) $\varphi = 90^\circ$ and (d) $\varphi = 0^\circ$. The direction of the optical polarization and electric-field distribution is shown on the left side. The coupling strength within the iron core region is set to zero. $\theta (=0.41\pi)$ is the axial phase difference between the TM_0 and HE_1^z modes in part d.

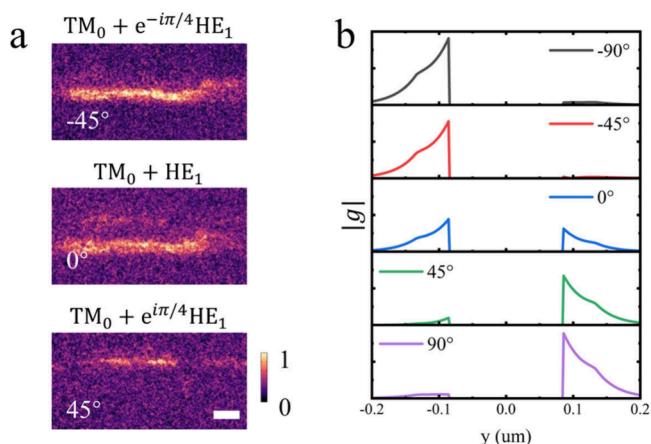


Figure 5. Polarization-dependent mode superposition. Experimental data (a) and theoretical simulations (b). $\varphi = 0^\circ$ represents optical polarization parallel to the electron beam. The scale bar is 200 nm.

Our findings reveal that MWCNTs not only effectively protect iron from oxidation but also provide a confined environment for plasmons, thereby enhancing mode densities. The insights gained from plasmon-mode superposition in iron-filled MWCNTs enable the development of enhanced nanosensors and tunable nanophotonic devices with potential applications in biosensing, optical signal processing, and integrated plasmonic circuits.

ASSOCIATED CONTENT

Supporting Information

The Supporting Information is available free of charge at <https://pubs.acs.org/doi/10.1021/acs.nanolett.5c01587>.

Details of experimental methods, simulations, dynamics images, and model analysis of the SP of iron-filled MWCNTs and additional data of near-field images of

hollow MWCNTs and theoretical prediction of silver-core-filled coaxial structures (PDF)

AUTHOR INFORMATION

Corresponding Authors

Dingguo Zheng – Beijing National Laboratory for Condensed Matter Physics, Institute of Physics, Chinese Academy of Sciences, Beijing 100190, China; orcid.org/0000-0002-7227-0048; Email: zdg@iphy.ac.cn

Jianqi Li – Beijing National Laboratory for Condensed Matter Physics, Institute of Physics, Chinese Academy of Sciences, Beijing 100190, China; School of Physical Sciences, University of Chinese Academy of Science, Beijing 100049, China; Songshan Lake Materials Laboratory, Dongguan 523808, China; orcid.org/0000-0002-4808-6347; Email: ljq@iphy.ac.cn

Huaxin Yang – Beijing National Laboratory for Condensed Matter Physics, Institute of Physics, Chinese Academy of Sciences, Beijing 100190, China; School of Physical Sciences, University of Chinese Academy of Science, Beijing 100049, China; Email: hxyang@iphy.ac.cn

Authors

Dong Yang – Beijing National Laboratory for Condensed Matter Physics, Institute of Physics, Chinese Academy of Sciences, Beijing 100190, China; School of Physical Sciences, University of Chinese Academy of Science, Beijing 100049, China; orcid.org/0009-0007-1931-6987

Siyuan Huang – Beijing National Laboratory for Condensed Matter Physics, Institute of Physics, Chinese Academy of Sciences, Beijing 100190, China; School of Physical Sciences, University of Chinese Academy of Science, Beijing 100049, China

Wentao Wang – Beijing National Laboratory for Condensed Matter Physics, Institute of Physics, Chinese Academy of Sciences, Beijing 100190, China; School of Physical Sciences,

University of Chinese Academy of Science, Beijing 100049, China; orcid.org/0009-0002-2071-2390

Jun Li – Beijing National Laboratory for Condensed Matter Physics, Institute of Physics, Chinese Academy of Sciences, Beijing 100190, China

Shuaishuai Sun – Beijing National Laboratory for Condensed Matter Physics, Institute of Physics, Chinese Academy of Sciences, Beijing 100190, China; orcid.org/0000-0002-9363-3901

Jiangbo Lu – School of Physics and Information Technology, Shaanxi Normal University, Xi'an 710119, China

Jieshan Qiu – College of Chemical Engineering, State Key Laboratory of Chemical Resource Engineering, Beijing University of Chemical Technology, Beijing 100029, China

Huanfang Tian – Beijing National Laboratory for Condensed Matter Physics, Institute of Physics, Chinese Academy of Sciences, Beijing 100190, China; School of Physical Sciences, University of Chinese Academy of Science, Beijing 100049, China

Complete contact information is available at:

<https://pubs.acs.org/10.1021/acs.nanolett.5c01587>

Author Contributions

D.Y. conducted the experimental work, while D.Y., H.Y. and D.Z. carried out the data processing and simulations for this study. J.Q. provided the iron-filled MWCNT samples. The remaining authors contributed by providing assistance with both the experimental and theoretical aspects of the research.

Notes

The authors declare no competing financial interest.

ACKNOWLEDGMENTS

This work was supported by the National Key R&D Program of China (Grants Nos. 2021YFA13011502, 2024YFA1408701, 2024YFA1408400, and 2024YFA1611303), the National Natural Science Foundation of China (Grant No. U22A6005), the Scientific Instrument Developing Project of the Chinese Academy of Sciences (Grant No. YJ-KYYQ20200055), and the Synergetic Extreme Condition User Facility (SECUF, <https://cstr.cn/31123.02.SECUF>).

REFERENCES

- (1) van de Haar, M. A.; Maas, R.; Brenny, B.; Polman, A. Surface Plasmon Polariton Modes in Coaxial Metal-Dielectric-Metal Waveguides. *New J. Phys.* **2016**, *18* (4), 043016.
- (2) Burgos, S. P.; de Waele, R.; Polman, A.; Atwater, H. A. A Single-Layer Wide-Angle Negative-Index Metamaterial at Visible Frequencies. *Nat. Mater.* **2010**, *9* (5), 407–412.
- (3) de Waele, R.; Burgos, S. P.; Atwater, H. A.; Polman, A. Negative Refractive Index in Coaxial Plasmon Waveguides. *Opt. Express* **2010**, *18* (12), 12770–12778.
- (4) Betzig, E.; Trautman, J. K. Near-Field Optics: Microscopy, Spectroscopy, and Surface Modification Beyond the Diffraction Limit. *Science* **1992**, *257* (5067), 189–195.
- (5) Bouhelier, A. Field-Enhanced Scanning near-Field Optical Microscopy. *Microsc. Res. Technol.* **2006**, *69* (7), 563–579.
- (6) Tugchinn, B. N.; Janunts, N.; Steinert, M.; Fasold, S.; Pertsch, T. Experimental Observation of the Short-Range Surface Plasmon Polariton Mode and Its Longitudinal Adiabatic Compression in a Metallic Wedge. *Opt. Express* **2021**, *29* (23), 37161–37174.
- (7) Colliex, C.; Kociak, M.; Stéphan, O. Electron Energy Loss Spectroscopy Imaging of Surface Plasmons at the Nanometer Scale. *Ultramicroscopy* **2016**, *162*, A1–A24.
- (8) Wu, Y.; Li, G.; Camden, J. P. Probing Nanoparticle Plasmons with Electron Energy Loss Spectroscopy. *Chem. Rev.* **2018**, *118* (6), 2994–3031.
- (9) Chen, J.; Albella, P.; Pirzadeh, Z.; Alonso-González, P.; Huth, F.; Bonetti, S.; Bonanni, V.; Åkerman, J.; Nogués, J.; Vavassori, P.; Dmitriev, A.; Aizpurua, J.; Hillenbrand, R. Plasmonic Nickel Nanoantennas. *Small* **2011**, *7* (16), 2341–2347.
- (10) Jiang, P.; Zheng, W.; Li, X.; Zhang, L.; Liu, Y.; Wang, Y.; Li, Y.; Gao, Y.; Yang, H.; Liu, Y.; Gong, Q.; Wu, C. Imaging and Controlling Ultrafast Electron Pulses Emitted from Plasmonic Nanostructures. *Nano Lett.* **2023**, *23* (16), 7327–7333.
- (11) Wu, Y.; Li, G.; Camden, J. P. Probing Nanoparticle Plasmons with Electron Energy Loss Spectroscopy. *Chem. Rev.* **2018**, *118* (6), 2994–3031.
- (12) Piazza, L.; Lummen, T. T. A.; Quiñonez, E.; Murooka, Y.; Reed, B. W.; Barwick, B.; Carbone, F. Simultaneous Observation of the Quantization and the Interference Pattern of a Plasmonic Near-Field. *Nat. Commun.* **2015**, *6* (1), 6407.
- (13) Liebrau, M.; Sivi, M.; Feist, A.; Lourenço-Martins, H.; Pazos-Pérez, N.; Alvarez-Puebla, R. A.; de Abajo, F. J. G.; Polman, A.; Ropers, C. Spontaneous and Stimulated Electron–Photon Interactions in Nanoscale Plasmonic near Fields. *Light Sci. Appl.* **2021**, *10* (1), 82.
- (14) Yurtsever, A.; Zewail, A. H. Direct Visualization of Near-Fields in Nanoplasmonics and Nanophotonics. *Nano Lett.* **2012**, *12* (6), 3334–3338.
- (15) Yurtsever, A.; van der Veen, R. M.; Zewail, A. H. Subparticle Ultrafast Spectrum Imaging in 4D Electron Microscopy. *Science* **2012**, *335* (6064), 59–64.
- (16) Zheng, D.; Huang, S.; Zhu, C.; Xu, P.; Li, Z.; Wang, H.; Li, J.; Tian, H.; Yang, H.; Li, J. Nanoscale Visualization of a Photoinduced Plasmonic Near-Field in a Single Nanowire by Free Electrons. *Nano Lett.* **2021**, *21* (24), 10238–10243.
- (17) Zheng, D.; Huang, S.; Zhu, C.; Li, Z.; Zhang, Y.; Yang, D.; Tian, H.; Li, J.; Yang, H.; Li, J. Enhancement of Lattice Dynamics by an Azimuthal Surface Plasmon on the Femtosecond Time Scale in Multi-Walled Carbon Nanotubes. *Nanoscale* **2022**, *14* (29), 10477–10482.
- (18) Barwick, B.; Flannigan, D. J.; Zewail, A. H. Photon-Induced near-Field Electron Microscopy. *Nature* **2009**, *462* (7275), 902–906.
- (19) Schröder, B.; Weber, T.; Yalunin, S. V.; Kiel, T.; Matyssek, C.; Sivi, M.; Schäfer, S.; von Cube, F.; Irsen, S.; Busch, K.; Ropers, C.; Linden, S. Real-Space Imaging of Nanotip Plasmons Using Electron Energy Loss Spectroscopy. *Phys. Rev. B* **2015**, *92* (8), 085411.
- (20) Fu, X.; Sun, Z.; Ji, S.; Liu, F.; Feng, M.; Yoo, B.-K.; Zhu, Y. Nanoscale-Femtosecond Imaging of Evanescent Surface Plasmons on Silver Film by Photon-Induced Near-Field Electron Microscopy. *Nano Lett.* **2022**, *22* (5), 2009–2015.
- (21) Meuret, S.; Lourenco-Martins, H.; Weber, S.; Houdellier, F.; Arbouet, A. Photon-Induced Near-Field Electron Microscopy of Nanostructured Metallic Films and Membranes. *ACS Photonics* **2024**, *11* (3), 977–984.
- (22) Kaplan, M.; Yoo, B.-K.; Tang, J.; Karam, T. E.; Liao, B.; Majumdar, D.; Baltimore, D.; Jensen, G. J.; Zewail, A. H. Photon-Induced Near-Field Electron Microscopy of Eukaryotic Cells. *Angew. Chem., Int. Ed.* **2017**, *56* (38), 11498–11501.
- (23) Flannigan, D. J.; Barwick, B.; Zewail, A. H. Biological Imaging with 4D Ultrafast Electron Microscopy. *Proc. Natl. Acad. Sci. U. S. A.* **2010**, *107* (22), 9933–9937.
- (24) Huang, S.; Xu, P.; Zheng, D.; Li, J.; Tian, H.; Yang, H.; Li, J. Plasmonic Near-Field Spatiotemporal Characterizations of an Asymmetric Copper Bowtie Nanostructure. *Appl. Phys. Lett.* **2023**, *122* (11), 111102.
- (25) Yurtsever, A.; Baskin, J. S.; Zewail, A. H. Entangled Nanoparticles: Discovery by Visualization in 4D Electron Microscopy. *Nano Lett.* **2012**, *12* (9), S027–S032.
- (26) Lummen, T. T. A.; Lamb, R. J.; Berruto, G.; LaGrange, T.; Dal Negro, L.; García de Abajo, F. J.; McGrouther, D.; Barwick, B.;

- Carbone, F. Imaging and Controlling Plasmonic Interference Fields at Buried Interfaces. *Nat. Commun.* **2016**, *7* (1), 13156.
- (27) Bao, J.; Zhou, Q.; Hong, J.; Xu, Z. Synthesis and Magnetic Behavior of an Array of Nickel-Filled Carbon Nanotubes. *Appl. Phys. Lett.* **2002**, *81* (24), 4592–4594.
- (28) Hang, B. T.; Hayashi, H.; Yoon, S.-H.; Okada, S.; Yamaki, J. Fe₂O₃-Filled Carbon Nanotubes as a Negative Electrode for an Fe–Air Battery. *J. Power Sources* **2008**, *178* (1), 393–401.
- (29) Li, J.; Moskovits, M.; Haslett, T. L. Nanoscale Electroless Metal Deposition in Aligned Carbon Nanotubes. *Chem. Mater.* **1998**, *10* (7), 1963–1967.
- (30) Yang, W.; Liu, X.; Yue, X.; Jia, J.; Guo, S. Bamboo-like Carbon Nanotube/Fe₃C Nanoparticle Hybrids and Their Highly Efficient Catalysis for Oxygen Reduction. *J. Am. Chem. Soc.* **2015**, *137* (4), 1436–1439.
- (31) Li, X.; Ni, L.; Zhou, J.; Xu, L.; Lu, C.; Yang, G.; Ding, W.; Hou, W. Encapsulation of Fe Nanoparticles into an N-Doped Carbon Nanotube/Nano Sheet Integrated Hierarchical Architecture as an Efficient and Ultra Stable Electrocatalyst for the Oxygen Reduction Reaction. *Nanoscale* **2020**, *12* (26), 13987–13995.
- (32) Yang, C.-K.; Zhao, J.; Lu, J. P. Magnetism of Transition-Metal/Carbon-Nanotube Hybrid Structures. *Phys. Rev. Lett.* **2003**, *90* (25), 257203.
- (33) Zhu, H.; Lin, H.; Guo, H.; Yu, L. Microwave Absorbing Property of Fe-Filled Carbon Nanotubes Synthesized by a Practical Route. *Mater. Sci. Eng., B* **2007**, *138* (1), 101–104.
- (34) Che, R.; Liang, C.; Shi, H.; Zhou, X.; Yang, X. Electron Energy-Loss Spectroscopy Characterization and Microwave Absorption of Iron-Filled Carbon-Nitrogen Nanotubes. *Nanotechnology* **2007**, *18* (35), 355705.
- (35) Song, J.; Wang, S.; He, Y.; Dai, Y.; Li, W.; Wu, H.; He, W.; Gu, A.; Guo, J.; Wen, J.; Boi, F. S. Unusual Radial Breathing Mode Signals in Cm-Scale Carbon Nanotube Buckypapers Filled with Fe₃C Single Crystals: Investigating the Role of Chirality. *Carbon Trends* **2022**, *8*, 100179.
- (36) Wroblewska, A.; Gordeev, G.; Duzynska, A.; Reich, S.; Zdrojek, M. Doping and Plasmonic Raman Enhancement in Hybrid Single Walled Carbon Nanotubes Films with Embedded Gold Nanoparticles. *Carbon* **2021**, *179*, 531–540.
- (37) Amirjani, A.; Tsoulos, T. V.; Sajjadi, S. H.; Antonucci, A.; Wu, S.-J.; Tagliabue, G.; Haghshenas, D. F.; Boghossian, A. A. Plasmon-Induced near-Infrared Fluorescence Enhancement of Single-Walled Carbon Nanotubes. *Carbon* **2022**, *194*, 162–175.
- (38) Zhao, Y.-M.; Hu, X.-G.; Chen, C.; Wang, Z.-H.; Wu, A.-P.; Zhang, H.-W.; Hou, P.-X.; Liu, C.; Cheng, H.-M. Plasmon-Enhanced Ultra-High Photoresponse of Single-Wall Carbon Nanotube/Copper/Silicon near-Infrared Photodetectors. *Nano Res.* **2024**, *17* (7), 5930–5936.
- (39) Fujita, T.; Chen, M.; Wang, X.; Xu, B.; Inoke, K.; Yamamoto, K. Electron Holography of Single-Crystal Iron Nanorods Encapsulated in Carbon Nanotubes. *J. Appl. Phys.* **2007**, *101* (1), 14323.
- (40) Sujak, M.; Djuhana, D. Investigation of Localized Surface Plasmon Resonance Properties of Non-Noble Metals: Fe, Ni, and Ni₈₀Fe₂₀. *Key Eng. Mater.* **2020**, *855*, 243–247.
- (41) Amirjani, A.; Haghshenas, D. F. Ag Nanostructures as the Surface Plasmon Resonance (SPR)-based Sensors: A Mechanistic Study with an Emphasis on Heavy Metallic Ions Detection. *Sens. Actuators, B* **2018**, *273*, 1768–1779.
- (42) Derkachova, A.; Kolwas, K.; Demchenko, I. Dielectric Function for Gold in Plasmonics Applications: Size Dependence of Plasmon Resonance Frequencies and Damping Rates for Nanospheres. *Plasmonics* **2016**, *11* (3), 941–951.
- (43) Han-Xun, Q.; Zhi-Yong, W.; Zu-Jin, S. H. I.; Zhen-Nan, G. U.; Jie-Shan, Q. I. U. Synthesis and Infrared Spectroscopy Characterization of Ferrocene-filled Double-walled Carbon Nanotubes. *Acta Phys.-Chim. Sin.* **2007**, *23* (9), 1451–1453.
- (44) Kim, H.; Sigmund, W. Iron Particles in Carbon Nanotubes. *Carbon* **2005**, *43* (8), 1743–1748.
- (45) Blank, V.; Buranova, Y.; Kulnitskiy, B.; Perezhogin, I. A.; Bagramov, R.; Dubitsky, G. Formation and Crystallographic Relations of Iron Phases and Iron Carbides inside the Carbon Nanotubes. *High Temp.-High Pressures* **2014**, *43*, 39–45.
- (46) Park, S. T.; Lin, M.; Zewail, A. H. Photon-Induced near-Field Electron Microscopy (PINEM): Theoretical and Experimental. *New J. Phys.* **2010**, *12* (12), 123028.